ADVANCED FUNCTIONAL MATERIALS
www.afm-journal.de

Modulating the Voltage Decay and Cationic Redox Kinetics of Li-Rich Cathodes via Controlling the Local Electronic Structure

Hung-Ling Yu, Kassa Belay Ibrahim, Po-Wei Chi, Yu-Hsuan Su, Wei-Tin Chen, Shao-Chin Tseng, Mau-Tsu Tang, Chi-Liang Chen, Horng-Yi Tang, Chih-Wen Pao, Kuei-Hsein Chen, Maw-Kuen Wu, and Heng-Liang Wu**

Li-rich layered oxide cathodes with conventional transition metal cation and unique oxygen anion redox reactions deliver high capacities in Li-ion batteries. However, the oxygen redox process causes the oxygen release, voltage fading/hysteresis, and sluggish electrochemical kinetics, which undermine the performance of these materials. By combining operando quick-scanning X-ray absorption spectroscopy with online gas chromatography, the effect of the local electronic structure is elucidated on the reaction mechanism and electrochemical kinetics of Li-rich cathodes. The local electronic structure of Li-rich cathodes varies with the excess Li (i.e., Li_2MnO_3 phase) and Ni contents. Compared to the Li-rich cathodes with higher amounts of Li_2MnO_3 phase (high excess lithium content (HLC) cathode), those with lower Li_2MnO_3 contents (low excess lithium content (LLC) cathode) exhibit reversible anion redox reactions and suppressed voltage hysteresis. The cation oxidation process of LLC cathode is kinetically slower than that of HLC cathode and the cation oxidation potential is shifted, likely due to the local coordination associated with different Li/O ratios. The obtained insights into the effect of local electronic structure on the reaction mechanism and kinetics provide a better understanding and control of Li-rich cathodes.

1. Introduction

Rechargeable Li-ion battery (LIB) technologies are employed in a wide range of applications, including portable devices, renewable energy infrastructures, and electrified transportation.[1–6] A significant improvement in the energy density of LIBs is needed to satisfy the growing energy demand. The specific energy density of LIBs is limited by the low specific capacity of cathodes such as lithium 3d tradition metal (TM) oxides ($LiTMO_2$, <200 mAh g^{-1}) that hinders the development of the next-generation LIBs. Thus, the efforts in searching for better cathode materials become pivotal. Cathodes based on Li-rich layered TM oxides with chemical formula $Li_{1+x}(Ni,Co,Mn)_{1-x}O_2$, have attracted great attentions, mainly due to their considerably high capacities.[3,4,7–11] $Li_{1.2}(Ni_{0.13}Co_{0.13}Mn_{0.54})O_2$ has been reported to deliver a specific charge capacity of ≈250 mAh g^{-1}.[2,12,13] Such high capacities arise from the conventional redox processes of TM cations and unique redox chemistry of O^{2-} anions.[4,14,15] However, Li-rich cathodes suffer from oxygen release, voltage fading/hysteresis, and poor electrochemical kinetics during cycling, which likely result from the oxygen redox reactions.[3,8,9,13,16–18]

Establishing the oxygen redox mechanism is essential to improve the unfavorable electrochemical properties of Li-rich cathodes. Previous studies suggested that the oxygen redox activity originates from the Li—O—Li configuration, which creates orphaned oxygen electrons (nonbonding O_{2p} bands) in Li-rich materials, making the labile Li—O—Li states available for

H.-L. Yu, K. B. Ibrahim, W.-T. Chen, K.-H. Chen, H.-L. Wu
Center for Condensed Matter Sciences
National Taiwan University
No. 1, Section 4, Roosevelt Road, Taipei City 10617, Taiwan
E-mail: hengliangwu@ntu.edu.tw

P.-W. Chi, Y.-H. Su, M.-K. Wu
Institute of Physics
Academia Sinica
No. 128, Sec. 2, Academia Rd., Nangang Dist., Taipei City 115201, Taiwan
E-mail: mkwu@phys.sinica.edu.tw

The ORCID identification number(s) for the author(s) of this article can be found under https://doi.org/10.1002/adfm.202112394.

DOI: 10.1002/adfm.202112394

W.-T. Chen, H.-L. Wu
Center of Atomic Initiative for New Materials
National Taiwan University
Taipei City 10617, Taiwan

S.-C. Tseng, M.-T. Tang, C.-L. Chen, C.-W. Pao
National Synchrotron Radiation Research Center
Hsinchu 30076, Taiwan

H.-Y. Tang
Department of Applied Chemistry
National Chi Nan University
Puli 545, Taiwan

K.-H. Chen
Institute of Atomic and Molecular Sciences
Academia Sinica
Taipei City 10617, Taiwan

oxygen redox reactions.[13,19,20] Bruce and coworkers reported that localized electron holes are created in oxygen anions at high voltage (>4.5 V) during the charge process.[13] Because oxygen anions with localized electron holes are unstable, they tend to form short covalent bonds with another oxygen anions or TM ions, which promote the migration of the TMs.[21,22] In turn, the TM migration could lead to a reshuffling of the electronic states, shifting the oxygen reduction potential to lower values during the discharge process.[4,22] House et al. showed that the TM migration occurs mostly in-plane in 3d Li-rich layered oxides, and results in the formation of vacancy clusters. The oxygen coordination environment is thus changed, which shifts the anion redox potential.[17] The irreversible oxygen release and redox reactions during the charge–discharge process result in the rearrangement and migration of TM ions from the TM to the Li layer, which play an essential role in the voltage fading and hysteresis of Li-rich cathodes .[17,23,24]

Li_2MnO_3 phase (space group *C*2/*m*) and $LiTMO_2$ phase (space group *R*-3*m*) are the building blocks of Li-rich layered TM oxides.[25,26] These two phases have different local coordination environments and exhibit different redox mechanisms. For instance, the oxygen redox reactions exhibit a sluggish electrochemical kinetics, which mainly occurs in the Li_2MnO_3 phase.[3] Several strategies such as doping/substituting cations and increasing the cation contents have been proposed to manipulate the local coordination structure and suppress the voltage decay.[16,27,28] Substituting different TM cations such as Mn and Ru in the $Li_{1.2}Ni_{0.2}TM_{0.6}O_2$ material has different impacts on the oxygen activation that could result from the interaction between TM and lattice oxygen.[29] In addition, the Li content in the TM layer influences the degree of oxygen loss and the electrochemical performance.[30] However, studies of the electrochemical kinetics of Li-rich cathodes are rare, and the effect of the Li_2MnO_3 phase on the TM and oxygen reaction rates remains unclear.

Our approach is to design the Li-rich layered TM oxide cathodes with different Li_2MnO_3 and Ni contents, such as $Li_{1.2}Ni_{0.13}Co_{0.13}Mn_{0.54}O_2$ (high excess lithium content, HLC) and $Li_{1.08}Ni_{0.34}Co_{0.08}Mn_{0.5}O_2$ (low excess lithium content, LLC) materials. The unfavorable electrochemical properties of Li-rich cathodes could be improved by optimizing the local electronic structure. We analyze the effect of excess Li on the reversibility of the cation and anion redox reactions of the Li-rich cathode using a combination of operando quick-scanning X-ray absorption fine structure (QXAFS) spectroscopy, X-ray diffraction (XRD), and online gas chromatography (GC), which enables monitoring the cation/anion redox kinetics and dynamic structure of the cathodes. The two Li-rich cathode materials synthesized in this study are composed of Li_2MnO_3 phase and $LiTMO_2$ phase, but exhibit different charge profiles. The LLC material shows that the reversible cation/anion redox reactions and voltage decay can be suppressed during cycling. The kinetics of the cation oxidation process of the LLC cathode is slower than that of the HLC cathode, suggesting that the local coordination structure plays a key role in the reaction kinetics. The obtained mechanistic insights into the reaction potential and the electrochemical kinetics of the cation and anion redox processes are crucial for improving the stability of Li-rich cathodes.

2. Results and Discussion

The structure of HLC and LLC materials synthesized by coprecipitation was characterized using XRD and HR-TEM. **Figure 1**a–c shows the XRD patterns and Rietveld refinements. The characteristic XRD peaks were indexed to Li_2MnO_3-like (space group *C*2/*m*) and $LiTMO_2$-like (space group *R*-3*m*) phases. Although previous studies indexed the XRD peaks of Li-rich cathodes based on structural model of rhombohedral solid solution,[31] the superstructure-associated XRD peaks resulting from cation ordering in the TM layer of the monoclinic structure were excluded. Thus, a monoclinic solid solution and a two-phase model were used to index the HLC cathode materials.[17,26] Since some of the XRD peaks of the LLC material could only be fitted to the R-3*m* space group (Figure S1, Supporting Information), the two-phase model provides a better fitting for both HLC and LLC structures examined in the present study. The Rietveld refinement results of the HLC material shows that the fractions of *C*2/*m* and *R*-3*m* space groups are 84.8% and 15.2%, whereas the corresponding fractions for the LLC structure are 56.8% and 43.2%, respectively. The fitting process is described in the Supporting Information, and the crystallographic parameters are listed in Tables S1–S4 in the Supporting Information.

SEM and HR-TEM measurements were used to further examine the morphology and crystal structure of HLC and LLC materials (Figure 1di). The representative HR-TEM images and selected area electron diffraction (SAED) patterns show the highly crystallized structures of HLC and LLC in Figure 1e,f,h,i, respectively. Overlapping electron diffraction (ED) patterns of the *C*2/*m* and *R*-3*m* structures along the $[103]_{C2/m}$ and $[001]_{R\text{-}3m}$ directions are obtained in HLC materials (Figure 1f), in agreement with previous studies.[25] The additional spots marked by yellow arrows in the ED patterns result from stacking faults.[32] Figure 1i shows the overlapping ED patterns of the LLC material along the $[\text{-}101]_{C2/m}$ and $[\text{-}441]_{R\text{-}3m}$ directions, indicating that the C2/m and *R*-3*m* structure are integrated in the structure. The crystal structures of the HLC and LLC materials are shown in Figures S2 and S3 in the Supporting Information.

We next examined the electrochemical properties of the HLC and LLC cathodes. **Figure 2**a–c shows the corresponding charge–discharge profiles and electrochemical performance. The HLC cathode gives specific charge and discharge capacities of 300 and 236 mAh g^{-1} in the initial cycle, respectively. The charge profile of the HLC cathode shows an extended plateau in the high-potential region (>4.4 V) in the first cycle, which is a typical feature of Li-rich layered oxide materials (Figure 2a).[3] The characteristic plateau associated with the anion oxidation process disappears during cycling, which could result from the irreversible anion redox process.[33–35] In contrast, the LLC cathode exhibits a shorter plateau in the high-potential region, likely as a result of the low Li content in the TM layers of LLC material (Figure 2b). Figure 2c shows that the cycling performance of HLC cathode fades in the subsequent cycles and exhibits a discharge capacity of 185 mAh g^{-1} after 50 cycles. The discharge capacity drops severely in the second cycle,[16,36] which could result from the irreversible surface oxygen loss in the first cycle.[17] A specific discharge capacity of ≈200 mAh g^{-1} is obtained after 50 cycles for the LLC cathode, showing an improved electrochemical stability.

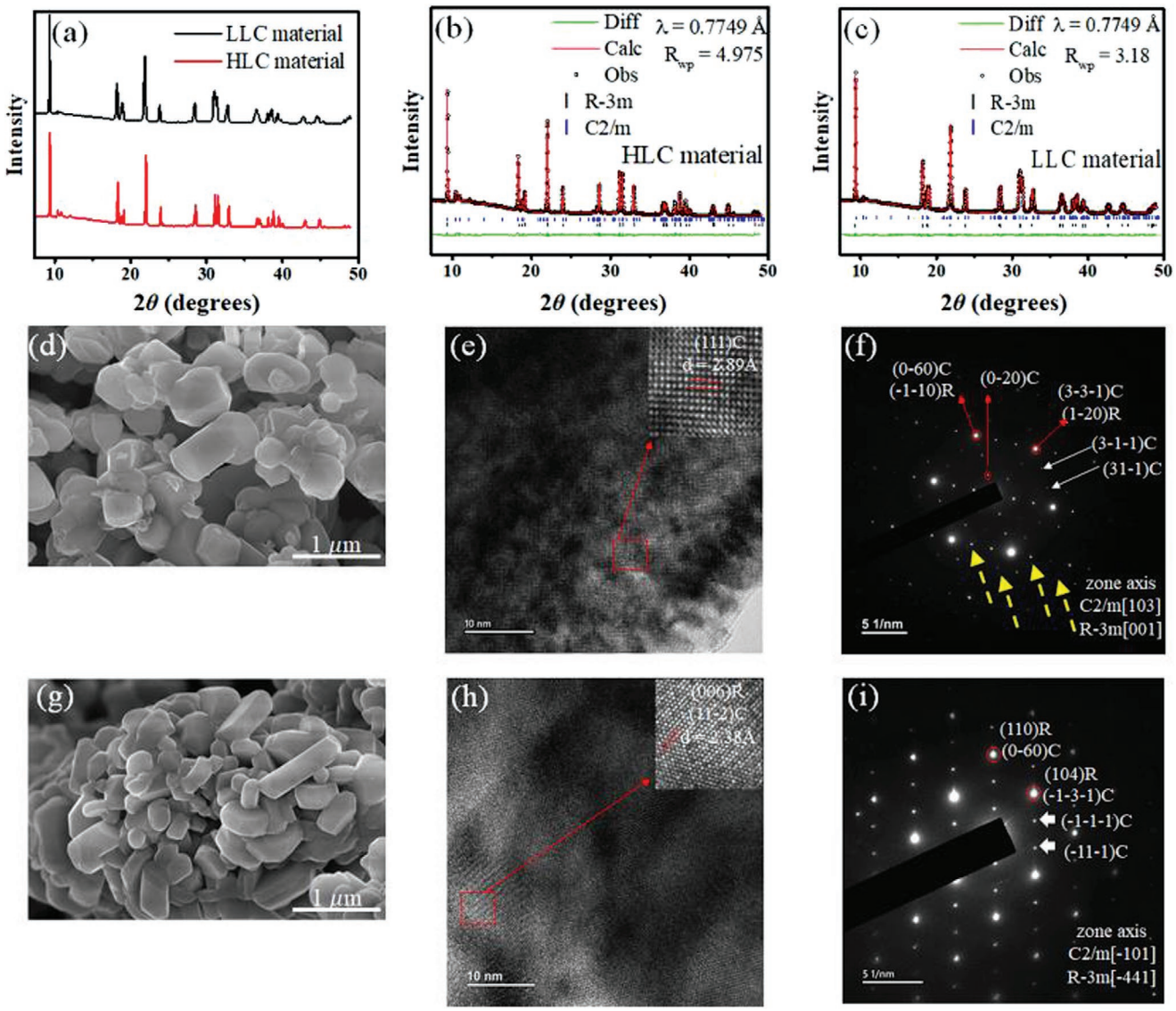

Figure 1. a) XRD patterns and Rietveld refinements of b) HLC and c) LLC materials. SEM, HR-TEM, and SAED images of d–f) HLC and g–i) LLC materials. C and R denote *C*2/*m* and *R*-3*m* space groups, respectively.

The differential capacity (dQ/dV, where V and Q are the voltage and capacity, respectively) plots of HLC and LLC cathode obtained in the first cycle show strong oxidation peaks at 3.9 and 4.5 V, respectively, corresponding to the TM cation (peaks A,C) and anion (O^{2-}) oxidation (peaks B,D) processes (Figure 2d,e).[37] During the anion oxidation process, the formation of oxygen dimers and released oxygen gas have been proposed.[4,13,17] Compared to the intensity of peak B in the plot of the HLC cathode, the weaker intensity of peak D could result from the lower Li content in the TM layer of the LLC material. More oxygen anions are oxidized in the HLC cathode. Since more oxygen redox reaction results in more specific capacity, the theoretical capacity of HLC cathode is higher than that of LLC cathode in the initial cycle. The additional reduction peak (peak E) drastically shifts toward the low-potential region during cycling (marked by arrow), suggesting that the voltage decay is severe in the HLC material. Because the reduction potential changes during cycling, the detailed reduction mechanism of the corresponding reduction peaks F-I is needed.

To study the effect of the Li content on the voltage fading during cycling, the voltage fading was quantitatively analyzed using the average potential (E) of the discharge profiles.[38] The charge or discharge energy was calculated as $\int_0^Q V(Q)dQ$, whereas the average potential was estimated from the relation $\frac{1}{Q}\int_0^Q V(Q)dQ = E/Q$. Figure 2f shows that the averaged voltage of the HLC cathode decreases continuously during cycling, resulting in severe voltage fading.

Nanostructured electrode materials have been proposed to improve the electrochemical performance of batteries.[39] The morphology and particle size of materials influence the electrochemical properties of materials.[39] The primary particle of HLC and LLC materials obtained from SEM images was

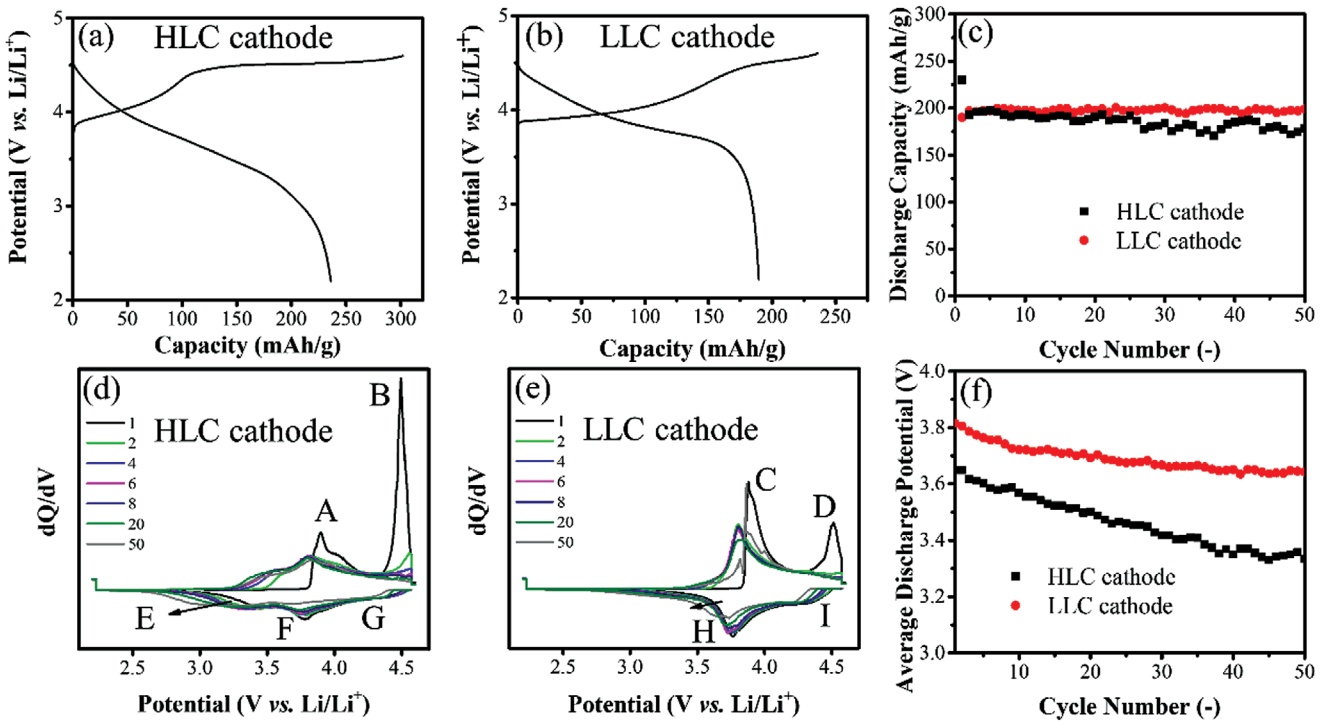

Figure 2. Charge–discharge profiles of a) HLC and b) LLC cathodes. c) Electrochemical performance of LLC and HLC cathodes obtained at a rate of 20 mA g^{-1} in the potential range of 4.6–2.2 V. dQ/dV plots of d) HLC and e) LLC cathodes. f) Average potential of charge–discharge profiles.

analyzed statistically using ImageJ (Figure S4a,b, Supporting Information). Figure S4c in the Supporting Information shows the N_2 adsorption–desorption isotherms of HLC and LLC materials. The detailed information regarding the statistical analysis of primary particle and the BET surface areas of HLC and LLC materials is provided in the supporting information. The dynamic light scattering (DLS) results could provide the general information regarding the particle size of materials. DLS results show that the averaged particles sizes of HLC and LLC materials are 736 and 798 nm, respectively, suggesting that the averaged particle size of HLC material is only ≈8% smaller than that of LLC material (Figure S4d, Supporting Information). Thus, the material with different particle size could change the electrochemical behavior slightly.

In order to investigate the effect of the Li_2MnO_3-like structure on the TM redox process, we examined operando X-ray absorption spectroscopy (XAS) of HLC and LLC cathodes obtained at representative potentials during the charge and discharge process. **Figure 3**a,b shows the representative operando Ni *K*-edge X-ray absorption near edge structure (XANES) spectra of HLC and LLC cathode in the first cycle. Before collecting the XAS spectrum, the battery was held at the specific potential for 30 min to ensure the completed reaction during the galvanostatic charge–discharge process. The absorption energy of white line (WL) position of HLC cathode at the Ni *K*-edge XANES spectra and the corresponding charge–discharge curves are shown in Figure 3c,d. Based on the WL position at the Ni *K*-edge XANES spectra of NiO (Ni^{2+}) and $LiNiO_2$ (Ni^{3+}), our results indicate that Ni is oxidized from Ni^{2+} to Ni^{4+} at potentials ranging from 2.2 to 4.4 V during charge process.[40] The oxidation state of Ni remains the constant at potentials above 4.4 V, consistent with the conclusion that the oxidation process is dominated by the anion (O^{2-}) oxidation process rather than the TM oxidation process in the high-potential region (>4.4 V).[13,41] During the discharge process, the absorption energy of WL position shifts to lower energy as a result of Ni reduction. The absorption energy of WL position changes monotonically during the discharge process, suggesting that the anion and TM reduction processes could be performed in similar potential regions.

Figure 3e,f shows the absorption energy of WL position of the LLC cathode at the Ni *K*-edge and the corresponding charge–discharge curves in the first cycle. The extended plateau in high-potential region is suppressed during the charge process, which could be associated with the lower Li content in the TM layer of the LLC cathode. Interestingly, the plots of the absorption energy of WL position exhibit two slopes (indicated by the dashed lines) during the discharge process (Figure 3f). The oxidation state of Ni remains constant from 4.6 to 4.4 V and then changes substantially below 4.4 V, likely resulting from the anion and TM reduction processes, respectively. The detailed operando Ni *K*-edge X-ray absorption spectra are shown in Figure S5 in the Supporting Information. Sequential anion and TM reduction processes were observed in the LLC cathode during the second cycle (Figure S6, Supporting Information), corresponding to the suppressed voltage fading. In addition, the Ni *K*-edge absorption energy of the LLC cathode is lower than that of the HLC cathode in the fully charged state, which is associated with the higher Ni content in the LLC cathode. Figure S7 in the Supporting Information shows XAS mappings at the Ni *K*-edge of HLC and LLC particles, obtained at 4.6 and 4.4 V during the discharge process. The fully charged state of Ni (Ni^{4+}) is uniformly distributed on the HLC particles at 4.6 V, in agreement with the operando XAS results.

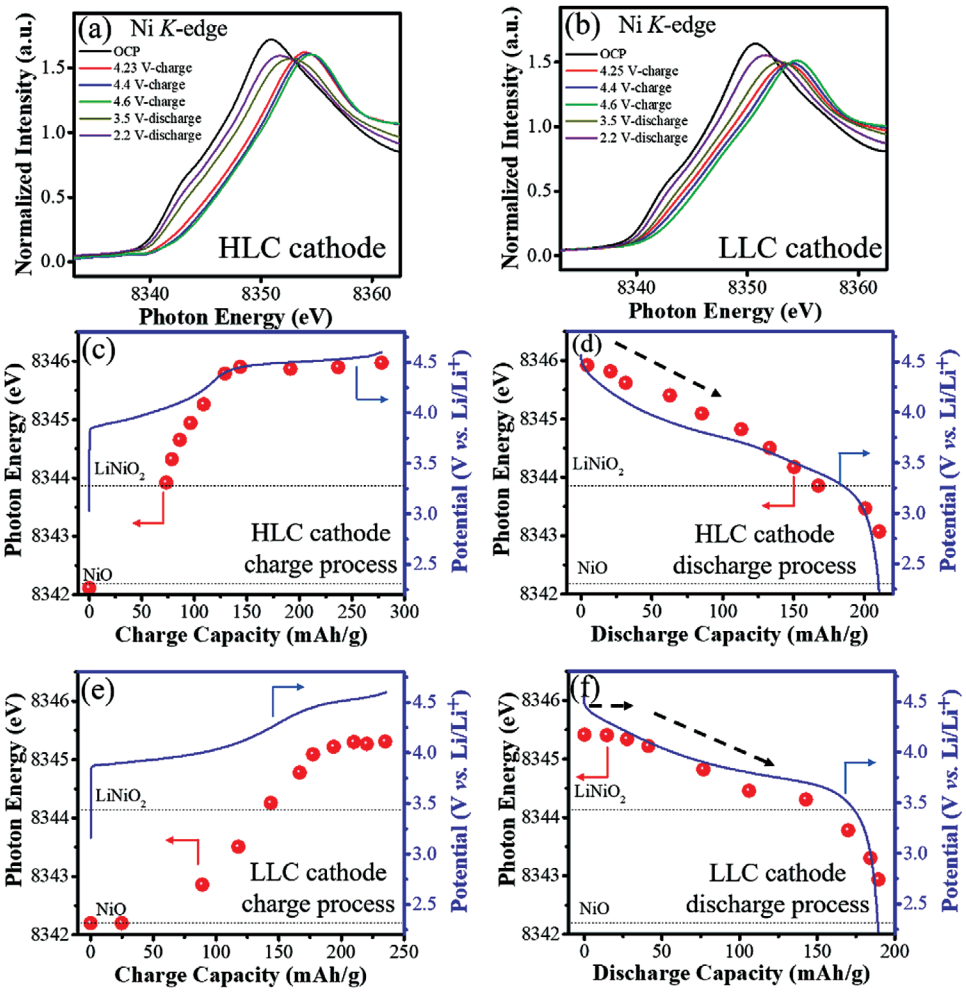

Figure 3. Operando Ni *K*-edge XANES spectra of a) HLC and b) LLC cathodes during cycling. The energy of white line position of c,d) HLC and e,f) LLC cathodes at the Ni *K*-edge XANES spectra and the corresponding charge–discharge curves. The absorption energy of white line position was defined over the half height of the normalized edge height.

Next, we studied the role of Co and Mn in the reaction mechanism of HLC and LLC cathode. The operando X-ray absorption spectra at the Co *K*-edge show the presence of Co^{3+} in the pristine materials and the Co redox process emerges to compensate the Li ion insertion and extraction (Figure S8, Supporting Information). The feature of Mn *K*-edge X-ray absorption spectra of the HLC and LLC cathodes changes with the isosbestic points (Figure S9, Supporting Information), and the energy position of the pre-edge peaks at 6538–6546 eV remains unchanged during cycling, which is consistent with previous studies (Figure S10, Supporting Information). Thus, only the electronic structure of the HLC and LLC cathodes changes, whereas the oxidation state of Mn is maintained during cycling.[42] The participation of TM cations in the electrochemical reactions and XANES at the Co and Mn *K*-edge are discussed in the Supporting Information.

The pre-edge peaks at 6538–6546 eV in the Mn *K*-edge XANES spectra are associated with the local structure ordering and the intensity reflects the deformation of MnO_6 octahedra.[43] Figure S11 in the Supporting Information shows that the intensity of the pre-edge peaks of the HLC cathode increases during the charge process and becomes much larger at potentials above 4.4 V. Compared to the Ni^{4+}—O and Co^{4+}—O bonds, the Mn^{4+}—O bond is less covalent, which could promote the formation of localized holes in the oxygen anions.[13] The distortion of MnO_6 octahedra likely results from the change in the Mn^{4+}–O interactions, while the Ni^{4+}—O/Co^{4+}—O interactions are invariant.[44] Thus, the anion redox process could result in a continuous change in the local structure of Mn. Also, MnO_6 octahedra are more distorted in the HLC than LLC cathode during the charge process. The variations in bond length and distortion of the HLC and LLC cathodes were evaluated using the operando Fourier transformed (FT) EXAFS spectra at the Mn *K*-edge (Figures S12 and S13, Supporting Information). The Debye–Waller factor of Mn-O in the two cathodes shows that severe distortion of MnO_6 octahedra in the HLC cathode results from the TM migration during the anion oxidation process.[43]

Lattice oxygen is known to compensate the charges beyond TM redox during the anion redox process which causes significant TM migration, irreversible surface oxygen loss and structural instability.[18,45] In order to study the extent of oxygen participation and the effect of the Li_2MnO_3-like structure on the oxygen reactivity, i.e., $2O^{2-} \rightarrow O_2 + 4e^-$, ex situ O *K*-edge X-ray

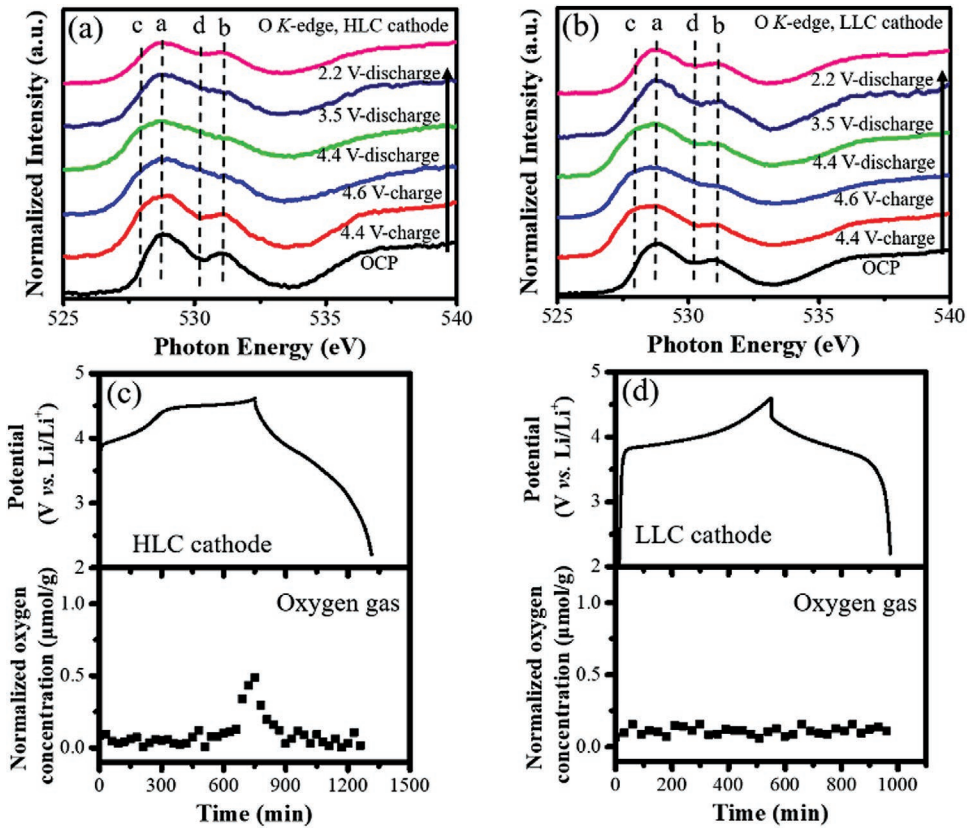

Figure 4. O *K*-edge X-ray absorption spectra of a) HLC and b) LLC cathodes obtained at different charge and discharge states. Online gas chromatography measurements of Li metal batteries with c) HLC and d) LLC cathodes and corresponding charge–discharge profiles during the first cycle.

absorption spectra and online GC were used to examine the TM-O hybridization and gas evolution. **Figure 4**a,b shows the O *K*-edge X-ray absorption spectra of HLC and LLC cathode obtained at representative potentials. The spectra were collected in TFY mode to study the bulk phenomena with limited interference from the cathode electrolyte interphase. The pre-edge peaks a and b in the spectra are associated with the transition from O_{1s} to TM_{3d}–O_{2p} orbitals.[29] During the charge process, peak *c* is formed at 527.8 eV when the potential reached 4.4 V, associated with the electron extraction from the TM_{3d}-O_{2p} (antibonding) band in the TM oxidation process (Figure 4a).[22] Upon charging the cathode from 4.4 to 4.6 V, the intensity of peak a remains constant and peak *d* is formed at ≈531 eV. Also, the intensity of peak *d* gradually increases during the further charge process. Peak *d* is assigned to oxidized oxygen, i.e., the electrons extracted from the nonbonding O_{2p} orbitals form new hole states in oxygen orbitals.[17] The O *K*-edge X-ray absorption spectra of the HLC cathode show that the intensity of peak d at 4.4 V remains unchanged during the discharge process, suggesting that the oxygen reduction potential shifts to lower potential.

In comparison, the O *K*-edge X-ray absorption spectra of the LLC cathode show a decrease in the intensity of peak d at 4.4 V during the discharge process. Thus, the anion reduction process could be carried out at a higher reduction potential in the LLC cathode, which is consistent with the operando Ni *K*-edge XAS results. The potential for the anion reduction process of the HLC cathode shifts to a lower potential, where the TM reduction process also takes place. The suppressed voltage fading is obtained in the LLC cathode.

The soft XAS results (O *K*-edge) suggest that the oxygen reactivities of HLC and LLC cathode might be different. Figure 4c,d shows online GC measurements of Li metal batteries with HLC and LLC cathodes and the corresponding charge–discharge profiles. The batteries were cycled between 3 and 4.6 V at a rate of 20 mA g^{-1}. The Li metal battery with HLC cathode exhibits that oxygen evolution is absent until 4.5 V and a released oxygen of 0.3 μmol g^{-1} is obtained at 4.55 V during the charge process. The oxygen concentration reaches 0.48 μmol g^{-1} at 4.6 V upon further charging, corresponding to the anion oxidation-related plateau in the charge profile of the HLC cathode (Figure 4c).[13] A lower oxygen release is observed for the Li metal battery assembled with the LLC cathode, which suggests a less significant oxygen participation in the charge process (Figure 4d). The amount of oxygen released in the HLC cathode decreases in the second cycle, as a result of irreversible oxygen redox reaction (Figure S14, Supporting Information).

The Li-rich cathodes with various excess lithium contents exhibit the irreversible reaction mechanism and voltage decay.[22,46,47] To further explore the effect of excess lithium content on the reaction mechanism of Li-rich layered TM oxide cathodes, the $Li(Ni_{0.5}Co_{0.2}Mn_{0.3})O_2$ (NCM523) material without excess lithium content was investigated in the present study. XRD peaks of the NCM523 material can be fitted to the *R*-3*m* space group (Figure S15a, Supporting Information). The

charge–discharge process and electrochemical performance of NCM523 material show that the cycling performance is stable in the potential range of 2.2–4.6 V (Figure S15b–d, Supporting Information). The crystallographic parameters are listed in Tables S5 in the Supporting Information. Operando XAS was used to study the reaction mechanism of NCM523 cathode. The white line position of Ni *K*-edge XANES spectra of NCM523 cathode changes monotonically during cycling (Figure S16, Supporting Information). Operando Mn *K*-edge XAS results of the NCM523 cathode show that distortion of MnO_6 octahedra and TM migration are suppressed in the NCM523 cathode (Figures S17 and S18, Supporting Information), which could originate from the eliminated anion reduction process. The O *K*-edge XAS (Figure S19, Supporting Information) and online gas chromatography measurements of NCM523 exhibit that no anion reaction is occurred. Thus, the excess lithium content of Li-rich layered TM oxide cathodes has major impacts on the reaction mechanism of Li-rich layered TM oxide cathodes.

Although the sluggish reaction kinetics originating from the lattice oxygen removal in the anion reduction process is well-known, the effect of excess Li on the dynamic structure of LLC and HLC materials remains unclear. Operando QXAFS spectroscopy measurements enable monitoring the time evolution of the TM redox process. **Figure 5**a,b shows the operando Ni *K*-edge X-ray absorption spectra of HLC and LLC cathodes during the charge–discharge process. The WL position of HLC cathode at the Ni *K*-edge XANES spectra shifts drastically to higher absorption energy when the cell is charged from 3.8 to 4.2 V (Figure 5c), and then changes slightly upon further charging above 4.2 V. In contrast, the WL position of LLC cathode gradually increases when the cell is charged from 3.8 to 4.2 V, suggesting that the reaction kinetics of HLC cathode is faster than that of LLC cathode (Figure 5d). Previous studies proposed that low-valent cations lead to a lower migration barrier for Li.[48] Thus, less TM cations in the TM layer of the HLC cathode could result in a faster Li extraction process, in agreement with the galvanostatic intermittent titration technique results (Figure S20, Supporting Information).

Interestingly, Ni is further oxidized at potentials ranging from 4.2 to 4.4 V. Compared to the HLC cathode, LLC cathode exhibits two Ni oxidation steps during the charge process and the Ni oxidation process occurs at higher potential region. Figure S21 in the Supporting Information shows that the Co redox potentials of the HLC and LLC cathode are also different. Sun et al. reported that the TM redox potential is determined by the energy gap between energy level of TM_{3d}-O_{2p} (or non-bonding O_{2p}) and Li redox reactions.[49] As the energy gap changes with the Li/O ratio, the lower Li/O ratio in the LLC

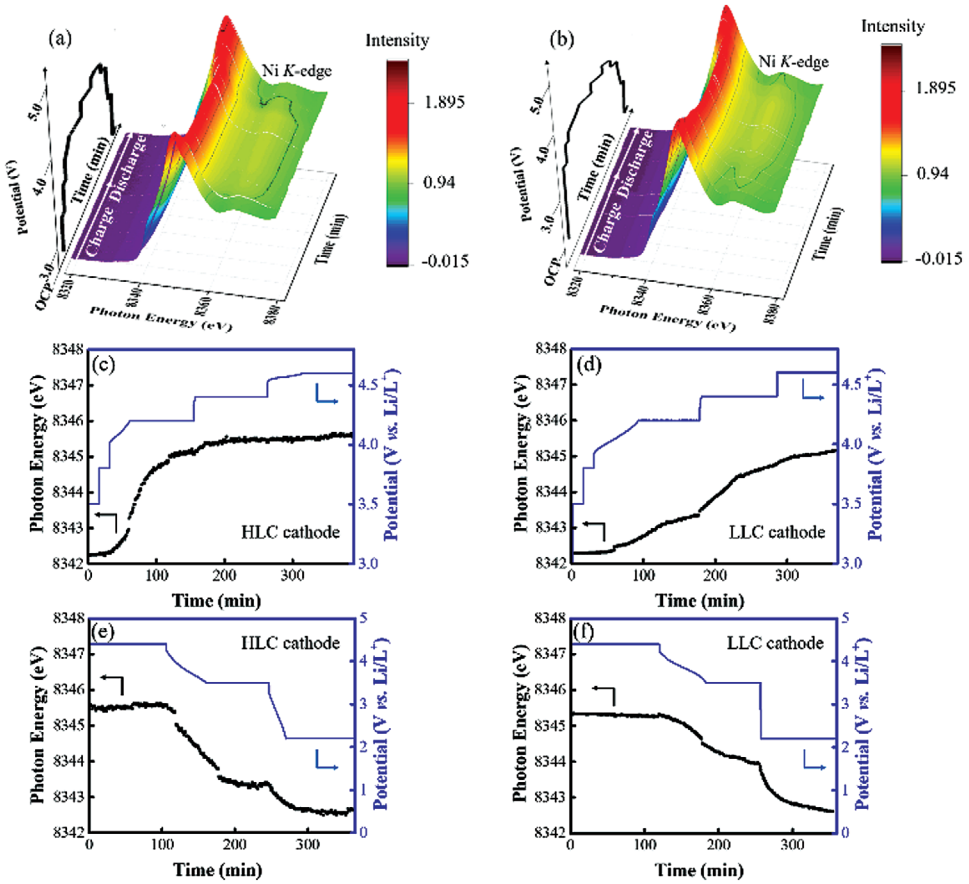

Figure 5. Operando Ni *K*-edge X-ray absorption near edge structure spectra of a) HLC and b) LLC cathodes during constant current/constant potential cycling. Ni *K*-edge absorption energies of c,e) HLC and d,f) LLC cathodes and corresponding potential profiles. The absorption energy of WL position was evaluated at the half height of the normalized edge height.

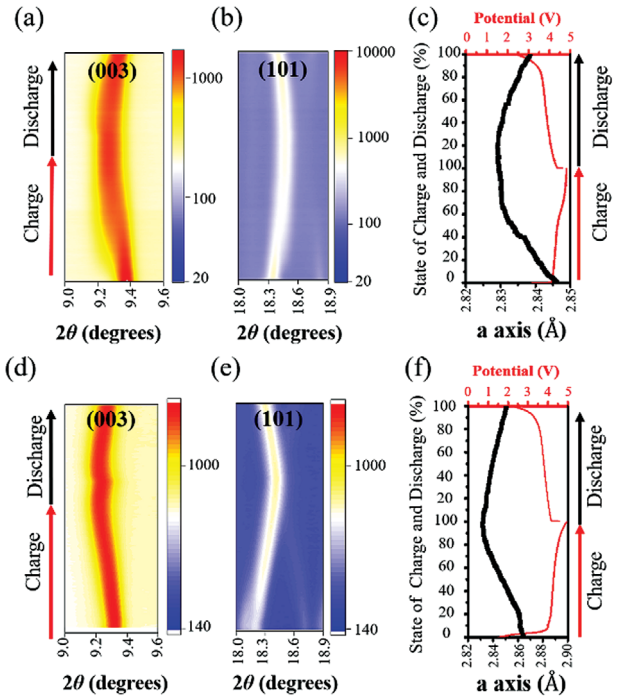

Figure 6. Contour plots of operando XRD results of a,b) HLC and d,e) LLC cathodes in representative 2θ regions and corresponding $(003)_{R\text{-}3m}$ and $(101)_{R\text{-}3m}$ XRD peaks (λ = 0.7749 Å). Calculated lattice parameters along the *a*-axis for c) HLC and f) LLC cathodes and corresponding charge–discharge curves at the cutoff voltage of 4.6 V.

cathode results in a higher potential for some of the TM ions. The stacking faults originating from the excess Li could also lead to a lower reaction potential.[20] During the discharge process from 4.4 to 3.8 V (Figure 5e,f), the Ni K-edge absorption energies decrease faster for HLC cathode than LLC cathode. The reduced local charge in the TM layer of the HLC material could promote a faster Li insertion.[48] The effect of kinetics of cation redox process on the electrochemical performance of HLC cathode than LLC cathode is discussed in the supporting information (Figure S22, Supporting Information).

The effect of the Li_2MnO_3-like structure on the phase evolution of the LLOs was further examined using operando XRD (**Figure 6**). Figure 6a,b,d,e shows the contour plots of the operando XRD data for HLC and LLC cathodes in the representative 2θ region and the corresponding $(003)_{R\text{-}3m}$ and $(101)_{R\text{-}3m}$ XRD peaks during cycling. The positions of these peaks shift during the charge and discharge process. The XRD results show the evolution of the $LiTMO_2$ phase of the HLC cathode. The detailed operando XRD results of the HLC and LLC cathode are provided in the Supporting Information (Figure S23, Supporting Information). Figure 6c,f shows the calculated lattice parameters along the *a*-axis of the HLC and LLC cathodes and the corresponding charge–discharge curves at the cutoff voltage of 4.6 V. The lattice parameters were calculated by fitting the XRD results with the rhombohedral *R*-3*m* space group. The changes in the *a*-axis of HLC cathode are associated with the TM redox reactions occurring below 4.4 V during the charge process (Figure 6c).[41] The *a*-axis of HLC cathode changes slightly from 4.4 to 4.6 V, consistent with the extended plateau in the corresponding charge curve. Since the oxidation state of the cations remains the same during the oxygen redox process and causes less pronounced changes in the lattice parameters. The characteristic structural evolution resulted from the TM and oxygen redox processes at different potential ranges are consistent with previous studies.[50,51] The calculated lattice parameter of the HLC and LLC cathodes follows the same trend when the potential varies from 2.2 to 4.4 V. The charge profile of the LLC cathode shows that the extended plateau is substantially suppressed. Thus, structural changes resulting from the oxygen redox process are barely observed for the LLC cathode in the 4.4–4.6 V potential window (Figure 6f).

Here, we further discuss the proposed reaction mechanism for HLC and LLC cathode. **Figure 7**a shows the proposed reaction mechanisms for HLC and LLC cathodes and the corresponding CV results. During the charge process in both cathodes, TM cation oxidation occurs first (region I), followed by oxygen anion oxidation (region II). Our results show a severe voltage decay in the HLC cathode, in which the anion reduction process can be carried out at lower potentials, together with the TM reduction process. On the other hand, sequential anion and TM reduction reactions take place in the LLC cathode during the discharge process.

In the following, we discuss possible reasons for the suppressed voltage decay in the LLC cathode. The TM layer is known to resemble a honeycomb-like structure, resulting in a large amount of Li_2MnO_3 phase (C2/m structure) in the HLC material. The lattice oxygen tends to form oxygen dimers,[21] which lead to metal-oxygen decoordination and TM migration. The voltage decay could originate from the TM migration during the lithiation process. Figure 7b shows a schematic illustration of the TM migration mechanism in HLC and LLC cathodes. Since HLC cathode has higher Li_2MnO_3 contents than LLC cathode, cation migration occurs much easier in HLC cathode and vacancies are clustered in the TM layer.[17] Thus, the different coordination environment of lattice oxygen ions could lead to the shift in oxygen reduction potential and voltage fading during the lithiation process. The dispersion of the Li_2MnO_3 phase in the $LiTMO_2$ phase framework has been reported to affect the TM migration process.[52] Also, previous studies have proposed that the voltage hysteresis and voltage fading can be limited by controlling the superstructure.[53] The lower fraction of Li_2MnO_3 phase is present in LLC cathode, which limits the TM migration and suppresses the voltage fading.

3. Conclusions

In summary, detailed spectroscopic and electrochemical analyses of HLC and LLC cathodes were carried out to elucidate the effect of the local electronic structure on the reaction mechanism and dynamic structure of Li-rich layered oxides in Li-ion batteries. The lower amounts of Li_2MnO_3 integrated with the $LiTMO_2$ phase in the LLC cathode show the improved electrochemical stability and suppressed voltage decay during cycling. Sequential anion and TM reduction processes are obtained during the discharge process. Interestingly, the kinetics of the TM redox process in the LLC cathode is slower than that

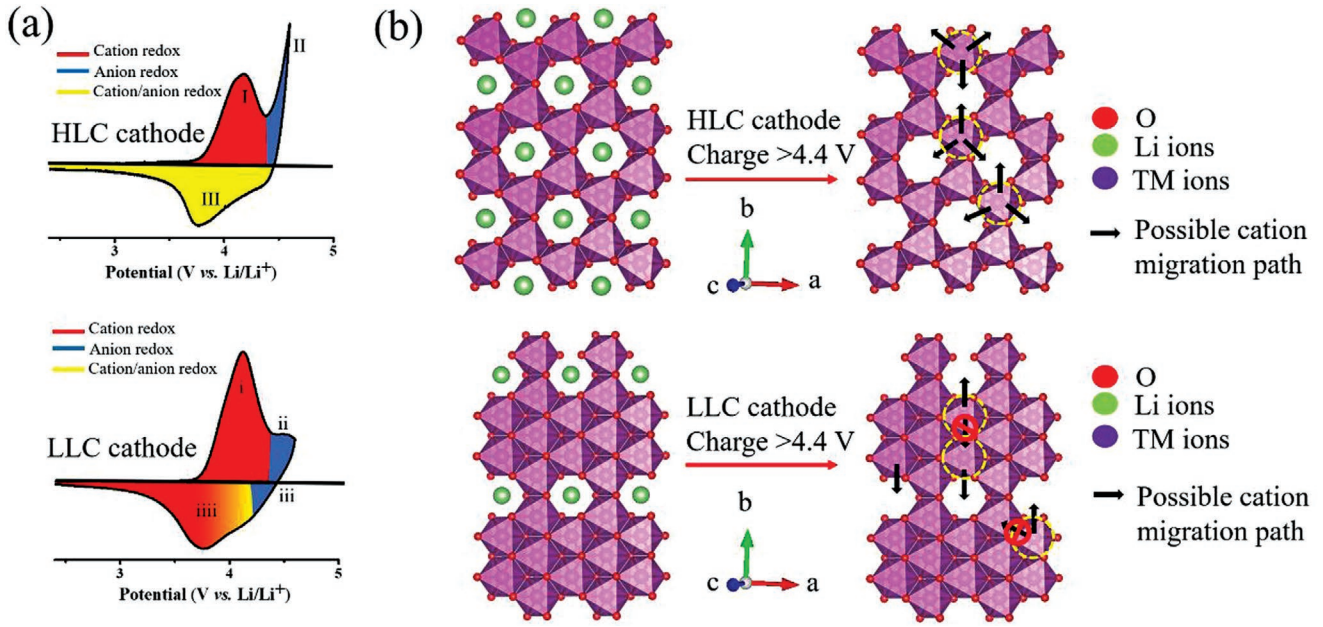

Figure 7. a) Reaction mechanisms of HLC and LLC cathodes and corresponding CV results. b) Schematic illustrations of cation migration pathways in HLC and LLC cathodes.

in the HLC cathode. In addition, the HLC cathode shows one Ni oxidation process in the potential window from 3.8 to 4.4 V, whereas the LLC cathode exhibits two Ni oxidation steps. Thus, the amount of Li_2MnO_3 phase affects both the reaction mechanism and kinetics of Li-rich cathodes. The evolution of the dynamic structure needs to be taken into account when addressing the cation and anion redox chemistry in Li-rich cathode. Our findings provide new insights into the reaction mechanism and kinetics of the TM redox reactions, showing that the electrochemical stability and kinetics of TM redox can be tuned by modifying the Li_2MnO_3 phase content.

4. Experimental Section

Material Synthesis and Characterization: Li-rich layered oxides (LLOs) including HLC and LLC materials were prepared by coprecipitation. The detailed synthesis procedure is shown in the supporting information. $Li(Ni_{0.5}Co_{0.2}Mn_{0.3})O_2$ (NCM523) was purchased from Gredmann. XRD measurements of the LLOs were performed at the TLS beamline 01C2 of the National Synchrotron Radiation Research Center (NSRRC), Hisnchu, Taiwan. The detailed synthesis process and XRD measurements are described in the Supporting Information. Scanning electron microscopy (SEM) images were obtained using FE-SEM (JEOL JSM-7600F) operated at 10 keV. Selected area electron diffraction (SAED) measurements were carried out using high-resolution transmission electron microscopy (HR-TEM, JEOL JEM-2100F) at 200 keV. The aperture used in the SAED measurement was ≈1 µm. X-ray absorption spectroscopy mapping measurements were performed at the TPS beamline 23A in NSRRC. The DLS measurements of HLC and LLC materials were conducted with NANO-ZS (Malvern Panalytical). HLC and LLC materials were dispersed in ethanol with a concentration of 0.5 mg mL^{-1} and sonicated for 15 min to obtain a well dispersed suspension. The suspension was measured at room temperature with an equilibrium time of 30 s. The N_2 adsorption–desorption isotherms were measured with ASAP 2020 (Micromeritics Co.) at 77 K.

Cathode Preparation and Electrochemical Measurements: The cathode slurry consisted of 80 wt% cathode materials, 10 wt% carbon black (Super P, Imerys Graphite & Carbon), and 10 wt% polyvinylidene fluoride (PVDF, UBIQ Technology Co., Ltd.) in N-methyl-2-pyrrolidone (NMP, 99%). The slurry was cast on an Al foil and the laminate was dried under vacuum at 90°C overnight. A coin cell (CR2032) consisting of a Li metal anode (300 µm thick), a separator (Celgard 2325, Celgard LLC Co.), and a LLOs cathode was assembled in an argon-filled glove box. The loading of active material was ≈14 mg cm^{-2}. Galvanostatic charge–discharge tests were performed between 4.6 and 2.2 V (versus Li/Li^+) at a current density of 20 mA g^{-1} using an Arbin cycler (LBTseries, Arbin Instruments). Cyclic voltammetry (CV) measurements were performed in a potential window from 2.2 to 4.6 V at a scan rate of 0.1 mV s^{-1} (600E Potentiostat, CHI Instruments, Inc.). The electrolyte used in the experiments was 1 M $LiPF_6$ in ethylene carbonate/diethyl carbonate (EC/DEC, 1:1 v/v, Sigma-Aldrich).

Operando XRD and QXAFS Measurements: Operando XRD and QXAFS measurements of LLOs were performed at the TLS 01C2 and TPS 44A beamlines in NSRRC, respectively. In the XRD measurements, the batteries were charged and discharged at a current density of 20 mA g^{-1}. The acquisition time of XRD pattern was 1 min. In the QXAFS experiment, the cell was charged and discharged at constant current (20 mA g^{-1}), followed by holding the potential at a given voltage to avoid hysteresis phenomena at each reaction step. The quick-scanning monochromator (Q-Mono) provides the capability of on-the-fly scan (q-scan), which can collect spectrum in sub-second time scale. A full QXAFS spectrum can be acquired in 500 ms using q-scan at the Q-Mono oscillation frequency of 2 Hz in TPS 44A endstation.[54] In order to increase the signal to noise ratio, each Ni, Co, Mn K-edge QXAFS spectrum was averaged by 120 spectra in this study, i.e., the time resolution was 60 s. The pure Mn, Co, and Ni foil were used to calibrate the incident photon energy. The QXAFS results obtained in transmission mode were analyzed with DEMETER software package.[55] Operando XAS measurements of NCM523 cathodes were performed at the TLS 17C beamline in NSRRC. Figure S24 in the Supporting Information shows the cell configuration for operando XRD and QXAFS measurements.

O K-Edge X-Ray Absorption Spectroscopy and GC Analyses: O K-edge XAS measurements were conducted at the TLS beamline 20A in NSRRC, Taiwan. Soft XAS measurements of the cathode materials were performed in total fluorescence yield (TFY) mode. The soft XAS spectra were collected with an exposure time of 50 s and averaged over five spectra. The cathode materials were rinsed with DEC solvent in an

argon-filled glove box and dried in vacuum prior to the measurements. In order to avoid exposing the cathode materials to ambient air, all the prepared cathode materials were kept under vacuum and transferred to a chamber filled with argon before the soft XAS measurements. A home-built online GC system (Agilent 7890) with a pulsed discharge helium ionization detector was used to analyze the gas products.[56,57] Since each GC measurement required 30 min, the released gases were accumulated in the cell for 30 min during the charge–discharge process prior to the GC measurements.

Statistical Analysis: The size of primary particle of HLC and LLC materials obtained from SEM images was analyzed statistically using ImageJ. 12 SEM images taken from three batches of HLC and LLC samples were analyzed. 60 primary particles were analyzed for each material. The projected areas of primary particles were 0.3 ± 0.25 and 0.26 ± 0.19 μm^2 (mean $\pm$ standard deviation) for HLC and LLC materials, respectively. Three BET measurements were done for each sample. The averaged BET surface areas of HLC and LLC materials are provided in the Supporting Information.

Supporting Information

Supporting Information is available from the Wiley Online Library or from the author.

Acknowledgements

This research was mainly supported by the Forward-Looking Research (Grant Number 110-0210-04-20-01), Ministry of Science and Technology (MOST), Taiwan (contract nos. 110-2124-M-001 -001 and 110-2113-M-002 -019 -MY3) and the Center of Atomic Initiative for New Materials, National Taiwan University, from the Featured Areas Research Center Program within the framework of the Higher Education Sprout Project by the Ministry of Education in Taiwan (108L9008). The authors thank C.-Y. Chung of the Institute of Atomic and Molecular Sciences, Academia Sinica for the operando cell development and Xiao-Yun Li at TPS 23A endstation, NSRRC for the technical support. The authors thank Yu-An Lin for the technical support in the GC measurement. TEM technical support from the Advanced Materials Characterization lab at Academia Sinica and Prof. Cheng-Yen Wen in National Taiwan University were acknowledged. The authors thank C.-Y. Ling and Y.-Y. Yang of Ministry of Science and Technology (National Taiwan University) for the assistance in FE-SEM experiments.

Conflict of Interest

The authors declare no conflict of interest.

Author Contributions

H.-L.Y. and H.-L.W. designed the experiments. H.-L.Y. contributed to electrochemical tests and TEM experiments. P.-W.C. and Y.-H.S. contributed to material synthesis. H.-L.Y. and W.-T.C. contributed to XRD experiments and Rietveld refinements. H.-L.Y., K.B.I., C.-L.C., C.-W.P., and H.-L.W. contributed to XAS experiments. H.-L.Y., S.-C.T., M.-T.T., and H.-L.W. contributed to XAS mapping experiments. H.-Y.T., K.-H.C., M.-K.W., and H.-L.W. contributed to conceptualization and resources. H.-L.W. supervised the project. H.-L.Y. and H.-L.W. wrote the manuscript. All the authors contributed to the discussion and provided feedback on the manuscript.

Data Availability Statement

The data that support the findings of this study are available on request from the corresponding author. The data are not publicly available due to privacy or ethical restrictions.

Keywords

cation redox kinetics, Li-ion batteries, Li-rich cathodes, oxygen redox reactions, quick-scanning X-ray absorption fine structure spectroscopy, voltage fading

Received: December 4, 2021
Revised: February 25, 2022
Published online: March 11, 2022

[1] M. Li, J. Lu, Z. Chen, K. Amine, *Adv. Mater.* **2018**, *30*, 1800561.
[2] S. Hu, A. S. Pillai, G. Liang, W. K. Pang, H. Wang, Q. Li, Z. Guo, *Electrochem. Energy Rev.* **2019**, *2*, 277.
[3] G. Assat, J.-M. Tarascon, *Nat. Energy* **2018**, *3*, 373.
[4] M. Li, T. Liu, X. Bi, Z. Chen, K. Amine, C. Zhong, J. Lu, *Chem. Soc. Rev.* **2020**, *49*, 1688.
[5] Z. Syum, T. Billo, A. Sabbah, B. Venugopal, S.-Y. Yu, F.-Y. Fu, H.-L. Wu, L.-C. Chen, K.-H. Chen, *ACS Sustainable Chem. Eng.* **2021**, *9*, 8970.
[6] T. Lin, T. U. Schulli, Y. Hu, X. Zhu, Q. Gu, B. Luo, B. Cowie, L. Wang, *Adv. Funct. Mater.* **2020**, *30*, 1909192.
[7] S. Zhao, K. Yan, J. Zhang, B. Sun, G. Wang, *Angew. Chem., Int. Ed.* **2021**, *60*, 2208.
[8] J. Wang, X. He, E. Paillard, N. Laszczynski, J. Li, S. Passerini, *Adv. Energy Mater.* **2016**, *6*, 1600906.
[9] E. Hu, X. Yu, R. Lin, X. Bi, J. Lu, S. Bak, K.-W. Nam, H. L. Xin, C. Jaye, D. A. Fischer, *Nat. Energy* **2018**, *3*, 690.
[10] P. Rozier, J. M. Tarascon, *J. Electrochem. Soc.* **2015**, *162*, A2490.
[11] H. Zheng, C. Zhang, Y. Zhang, L. Lin, P. Liu, L. Wang, Q. Wei, J. Lin, B. Sa, Q. Xie, D.-L. Peng, *Adv. Funct. Mater.* **2021**, *31*, 2100783.
[12] X. Ding, Y.-X. Li, M.-M. Deng, S. Wang, Y. Aqsa, Q. Hu, C.-H. Chen, *J. Alloys Compd.* **2019**, *791*, 100.
[13] K. Luo, M. R. Roberts, R. Hao, N. Guerrini, D. M. Pickup, Y.-S. Liu, K. Edström, J. Guo, A. V. Chadwick, L. C. Duda, P. G. Bruce, *Nat. Chem.* **2016**, *8*, 684.
[14] B. Li, D. Xia, *Adv. Mater.* **2017**, *29*, 1701054.
[15] L. Wang, A. Dai, W. Xu, S. Lee, W. Cha, R. Harder, T. Liu, Y. Ren, G. Yin, P. Zuo, *J. Am. Chem. Soc.* **2020**, *142*, 14966.
[16] P. K. Nayak, J. Grinblat, M. Levi, E. Levi, S. Kim, J. W. Choi, D. Aurbach, *Adv. Energy Mater.* **2016**, *6*, 1502398.
[17] R. A. House, G. J. Rees, M. A. Pérez-Osorio, J.-J. Marie, E. Boivin, A. W. Robertson, A. Nag, M. Garcia-Fernandez, K.-J. Zhou, P. G. Bruce, *Nat. Energy* **2020**, *5*, 777.
[18] S. Ramakrishnan, B. Park, J. Wu, W. Yang, B. D. McCloskey, *J. Am. Chem. Soc.* **2020**, *142*, 8522.
[19] D.-H. Seo, J. Lee, A. Urban, R. Malik, S. Kang, G. Ceder, *Nat. Chem.* **2016**, *8*, 692.
[20] H. Zhuo, Y. Liu, Z. Wang, A. Zhang, Z. Li, Z. Ren, X. Liu, H. Peng, L. Wang, J. Shi, *Nano Energy* **2021**, *83*, 105812.
[21] W. E. Gent, I. I. Abate, W. Yang, L. F. Nazar, W. C. Chueh, *Joule* **2020**, *4*, 1369.
[22] W. E. Gent, K. Lim, Y. Liang, Q. Li, T. Barnes, S.-J. Ahn, K. H. Stone, M. McIntire, J. Hong, J. H. Song, *Nat. Commun.* **2017**, *8*, 2091.
[23] H. Koga, L. Croguennec, M. Ménétrier, P. Mannessiez, F. Weill, C. Delmas, *J. Power Sources* **2013**, *236*, 250.
[24] W. Zuo, M. Luo, X. Liu, J. Wu, H. Liu, J. Li, M. Winter, R. Fu, W. Yang, Y. Yang, *Energy Environ. Sci.* **2020**, *13*, 4450.
[25] H. Yu, R. Ishikawa, Y. G. So, N. Shibata, T. Kudo, H. Zhou, Y. Ikuhara, *Angew. Chem.* **2013**, *125*, 6085.
[26] W. K. Pang, H.-F. Lin, V. K. Peterson, C.-Z. Lu, C.-E. Liu, S.-C. Liao, J.-M. Chen, *Chem. Mater.* **2017**, *29*, 10299.
[27] C. Laisa, A. N. Kumar, S. S. Chandrasekaran, P. Murugan, N. Lakshminarasimhan, R. Govindaraj, K. Ramesha, *J. Power Sources* **2016**, *324*, 462.

[28] J.-L. Shi, J.-N. Zhang, M. He, X.-D. Zhang, Y.-X. Yin, H. Li, Y.-G. Guo, L. Gu, L.-J. Wan, *ACS Appl. Mater. Interfaces* **2016**, *8*, 20138.
[29] J. Xu, M. Sun, R. Qiao, S. E. Renfrew, L. Ma, T. Wu, S. Hwang, D. Nordlund, D. Su, K. Amine, J. Lu, B. D. McCloskey, W. Yang, W. Tong, *Nat. Commun.* **2018**, *9*, 947.
[30] T. Arunkumar, Y. Wu, A. Manthiram, *Chem. Mater.* **2007**, *19*, 3067.
[31] C. Genevois, H. Koga, L. Croguennec, M. Ménétrier, C. Delmas, F. Weill, *J. Phys. Chem. C* **2015**, *119*, 75.
[32] A. Boulineau, L. Croguennec, C. Delmas, F. Weill, *Chem. Mater.* **2009**, *21*, 4216.
[33] H. Pan, S. Zhang, J. Chen, M. Gao, Y. Liu, T. Zhu, Y. Jiang, *Mol. Syst. Des. Eng.* **2018**, *3*, 748.
[34] P. K. Nayak, E. M. Erickson, F. Schipper, T. R. Penki, N. Munichandraiah, P. Adelhelm, H. Sclar, F. Amalraj, B. Markovsky, D. Aurbach, *Adv. Energy Mater.* **2018**, *8*, 1702397.
[35] S. Zhao, Z. Guo, K. Yan, S. Wan, F. He, B. Sun, G. Wang, *Energy Storage Mater.* **2020**, *34*, 716.
[36] Z. Sun, L. Xu, C. Dong, H. Zhang, M. Zhang, Y. Ma, Y. Liu, Z. Li, Y. Zhou, Y. Han, Y. Chen, *Nano Energy* **2019**, *63*, 103887.
[37] W. Lee, S. Muhammad, C. Sergey, H. Lee, J. Yoon, Y. M. Kang, W. S. Yoon, *Angew. Chem., Int. Ed.* **2020**, *59*, 2578.
[38] M. Bettge, Y. Li, K. Gallagher, Y. Zhu, Q. Wu, W. Lu, I. Bloom, D. P. Abraham, *J. Electrochem. Soc.* **2013**, *160*, A2046.
[39] S.-L. Cui, M.-Y. Gao, G.-R. Li, X.-P. Gao, *Adv. Energy Mater.* **2021**, *12*, 2003885.
[40] H. Koga, L. Croguennec, M. Ménétrier, P. Mannessiez, F. Weill, C. Delmas, S. Belin, *J. Phys. Chem. C* **2014**, *118*, 5700.
[41] S. Muhammad, H. Kim, Y. Kim, D. Kim, J. H. Song, J. Yoon, J.-H. Park, S.-J. Ahn, S.-H. Kang, M. M. Thackeray, *Nano Energy* **2016**, *21*, 172.
[42] M. Oishi, T. Fujimoto, Y. Takanashi, Y. Orikasa, A. Kawamura, T. Ina, H. Yamashige, D. Takamatsu, K. Sato, H. Murayama, *J. Power Sources* **2013**, *222*, 45.
[43] D. Buchholz, J. Li, S. Passerini, G. Aquilanti, D. Wang, M. Giorgetti, *ChemElectroChem* **2015**, *2*, 85.
[44] X. Yu, Y. Lyu, L. Gu, H. Wu, S. M. Bak, Y. Zhou, K. Amine, S. N. Ehrlich, H. Li, K. W. Nam, *Adv. Energy Mater.* **2014**, *4*, 1300950.
[45] M. Gu, I. Belharouak, J. Zheng, H. Wu, J. Xiao, A. Genc, K. Amine, S. Thevuthasan, D. R. Baer, J.-G. Zhang, *ACS Nano* **2013**, *7*, 760.
[46] M. Oishi, C. Yogi, I. Watanabe, T. Ohta, Y. Orikasa, Y. Uchimoto, Z. Ogumi, *J. Power Sources* **2015**, *276*, 89.
[47] X. Yang, X. Wang, Q. Wei, H. Shu, L. Liu, S. Yang, B. Hu, Y. Song, G. Zou, L. Hu, L. Yi, *J. Mater. Chem.* **2012**, *22*, 19666.
[48] K. Kang, G. Ceder, *Phys. Rev. B* **2006**, *74*, 094105.
[49] G. Sun, F. D. Yu, C. Zhao, R. Yu, S. Farnum, G. Shao, X. Sun, Z. B. Wang, *Adv. Funct. Mater.* **2021**, *31*, 2002643.
[50] D. Mohanty, S. Kalnaus, R. A. Meisner, K. J. Rhodes, J. Li, E. A. Payzant, D. L. Wood III, C. Daniel, *J. Power Sources* **2013**, *229*, 239.
[51] L. Simonin, J.-F. Colin, V. Ranieri, E. Canévet, J.-F. Martin, C. Bourbon, C. Baehtz, P. Strobel, L. Daniel, S. Patoux, *J. Mater. Chem.* **2012**, *22*, 11316.
[52] J. Bareño, M. Balasubramanian, S. H. Kang, J. G. Wen, C. H. Lei, S. V. Pol, I. Petrov, D. P. Abraham, *Chem. Mater.* **2011**, *23*, 2039.
[53] R. A. House, U. Maitra, M. A. Pérez-Osorio, J. G. Lozano, L. Jin, J. W. Somerville, L. C. Duda, A. Nag, A. Walters, K.-J. Zhou, *Nature* **2020**, *577*, 502.
[54] C.-W. Pao, J.-L. Chen, J.-F. Lee, M.-C. Tsai, C.-Y. Huang, C.-C. Chiu, C.-Y. Chang, L.-C. Chiang, Y.-S. Huang, *J. Synchrotron Radiat.* **2021**, *28*, 930.
[55] B. Ravel, M. Newville, *J. Synchrotron Radiat.* **2005**, *12*, 537.
[56] T.-C. Chou, C.-C. Chang, H.-L. Yu, W.-Y. Yu, C.-L. Dong, J.-J. Velasco-Vélez, C.-H. Chuang, L.-C. Chen, J.-F. Lee, J.-M. Chen, *J. Am. Chem. Soc.* **2020**, *142*, 2857.
[57] C.-A. Lo, C.-C. Chang, Y.-W. Tsai, S.-K. Jiang, B. J. Hwang, C.-Y. Mou, H.-L. Wu, *ACS Appl. Energy Mater.* **2021**, *4*, 5132.